

Photoluminescence in amorphous MgSiO_3 silicate

S. P. Thompson^{1*}, J. E. Parker¹, S. J. Day^{1,2}, L. D. Connor¹, A. Evans²

¹*Diamond Light Source, Harwell Science and Innovation Campus, Chilton, Didcot, Oxon OX11 0QX, UK*

²*Astrophysics Group, Keele University, Keele, Staffordshire ST5 5BG, UK*

Accepted 1988 December 15. Received 1988 December 14; in original form 1988 October 11

ABSTRACT

Samples of Amorphous MgSiO_3 annealed at temperature steps leading up to their crystallisation temperature show a rise in photoluminescence activity, peaking at $\sim 450^\circ\text{C}$. The photoluminescence band has a main peak at 595 nm and a weaker peak at 624 nm. We present laboratory data to show that the maximum in photoluminescence activity is related to substantial structural reordering that occurs within a relatively narrow temperature range. We attribute the origin of the photoluminescence to non-bridging oxygen hole centre defects, which form around ordered nano-sized domain structures as a result of the breakup of tetrahedral connectivity in the disordered inter-domain network, aided by the loss of bonded OH. These defects are removed as crystallisation progresses, resulting in the decrease and eventual loss of photoluminescence. Thermally processed hydrogenated amorphous silicate grains could therefore represent a potential carrier of extended red emission.

Key words: circumstellar matter: stars; ISM: general; radiation mechanisms: non-thermal; methods: laboratory.

1 INTRODUCTION

Extended red emission (ERE) is a broad ($\Delta\lambda \sim 60\text{--}120$ nm), featureless emission band with a peak wavelength between 600 and 850 nm first detected in the spectrum of HD 44179 (the Red Rectangle; Schmidt et al. 1980). ERE is commonly seen in environments where both dust and UV photons are present (Witt & Vijh 2004) and has been detected in reflection nebulae, dark nebulae, cirrus clouds, planetary nebulae, H II regions, novae, the diffuse interstellar medium (ISM), and the halos and high galactic latitude interstellar clouds of galaxies (e.g. Witt & Schild 1988; Witt & Boroson 1990; Scott et al. 1994; Szomoru & Guhathakurta 1998; Smith & Witt 2002; Rhee et al. 2007; Berné et al. 2008; Witt et al. 2008). Darbon et al. (1999) showed that the peak wavelength and width of the ERE band are correlated, while Smith & Witt (2002) showed that the peak wavelength also correlates with the density of the UV radiation field in a given ERE source. Examples of ERE illustrating the observational variation between different environments are shown in Fig. 1.

Since many solids emit visible luminescence when exposed to UV light, it is assumed that ERE is a photoluminescence (PL)¹ process powered by far-UV photons. In the ISM, $\sim 4\%$ of the energy absorbed by dust at wavelengths < 550 nm is emitted in the form of ERE, suggesting the car-

rier must be a major component of the interstellar grain population. The ERE carrier may have originally condensed in the circumstellar environment of proto-planetary and planetary nebulae and subsequently been ejected into the ISM (Witt et al. 1998). To survive the journey through the ISM and to spread throughout the halo of the Galaxy requires a robust carrier material. The intrinsic quantum yield of ERE may be as high as $\sim 50\%$ with its carrier intercepting $\sim 20\%$ of the photons absorbed by interstellar dust in the 90–550 nm range (Smith & Witt 2002), which therefore limits the chemical composition of the ERE carrier to the few elements that are both abundant and highly depleted, i.e. C, Fe, Si and Mg. Since metals do not produce PL, the remaining possibilities are C and Si bearing solids.

The physical nature of the ERE carrier is still contentious and various potential carriers have been proposed. These include hydrogenated amorphous carbon (Duley 1985; Duley & Williams 1988; Witt & Schild 1988; Furton & Witt 1992; Duley et al. 1997; Seahra & Duley 1999; Duley 2001; Godard & Dartois 2010), quenched carbonaceous composites (Sakata et al. 1992), C_{60} (Webster 1993), diamond (Duley 1988; Chang et al. 2006), embedded polycyclic aromatic hydrocarbon molecules (Wada et al. 2009), isolated dehydrogenated carbon clusters (Kurth et al. 2013) and silicon nanoparticles (Witt et al. 1998; Ledoux et al. 1998; Smith & Witt 2002). In a 2003 review, Draine (2003) noted that, while a number of these proposed identifications have been ruled out, the arguments against them are not conclusive. The fact that evidence for ERE was found in C-rich plan-

* E-mail: stephen.thompson@diamond.ac.uk

¹ A list of uncommon acronyms is given in the appendix.

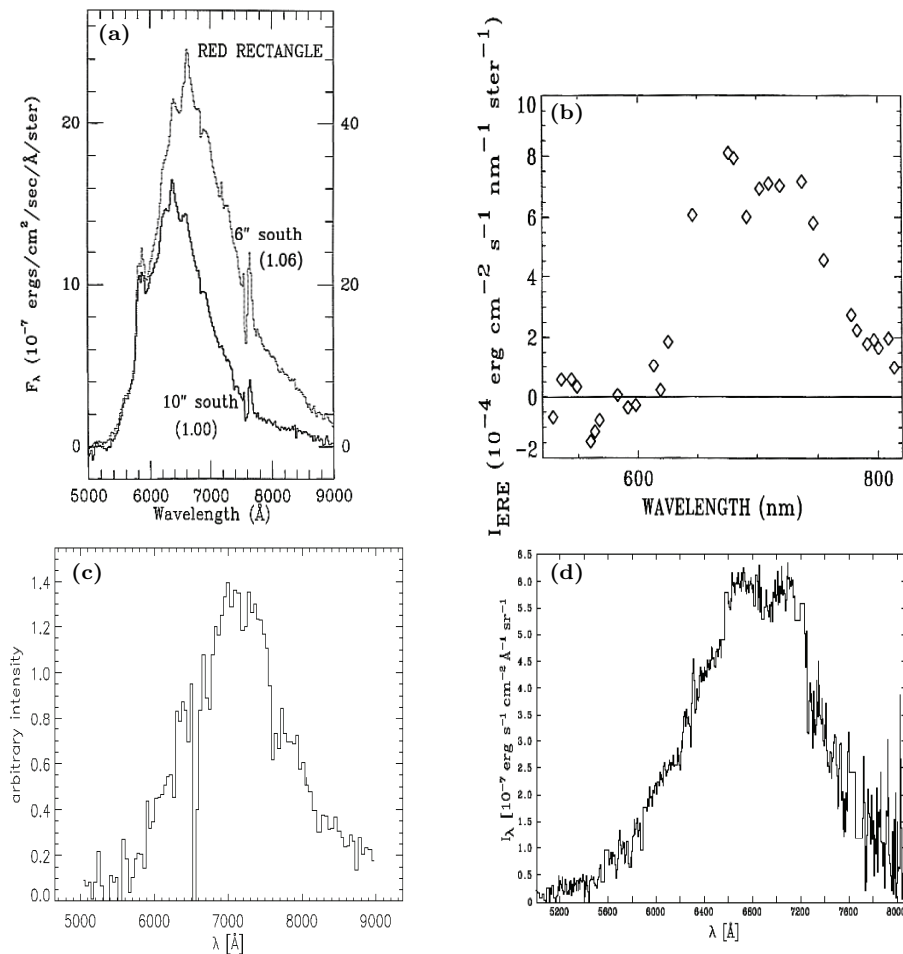


Figure 1. Observed ERE for (a) the Red Rectangle (from *Spectroscopy of extended red emission in reflection nebulae*, Witt, A. N., Boroson, T. A., *Astrophysical Journal*, 1990, 355, 182); (b) the planetary nebula NGC7027 (from *Extended red emission from dust in planetary nebulae*, Furton, D. G., Witt, A. N., 1992, *Astrophysical Journal*, 1992, 386, 587); (c) the NGC2327 reflection nebula (from *Extended Red Emission in the Diffuse Interstellar Medium*, Gordon, K. D., Witt, A. N., Friedmann, B. C. *Astrophysical Journal*, 1998, 498, 522) and (d) the north-western filament of the reflection nebula NGC 7023 (A. N. Witt personal communication, see also Witt et al. 2006). Figs. 1a-c reproduced by permission of the AAS.

etary nebulae (Furton & Witt 1992) initially pointed to a carbonaceous carrier, but there appears to be no correlation between the $3.3 \mu\text{m}$ UIR feature, generally attributed to PAH's, and the ERE in the Red Rectangle (Kerr et al. 1999); while amorphous carbon struggles to meet both efficiency and spectral constraints (Godard & Dartois 2010). Later Infrared Space Observatory (ISO) observations of C-rich planetaries showed the presence of strong crystalline silicate features (Waters et al. 1998). However, ERE has not been observed in O-rich planetaries, appearing to make a straightforward association with O-rich materials difficult, particularly since the Red Rectangle, which is the most prominent ERE source with local dust production, is a C-rich environment.

Nevertheless silicates are a well known and abundant dust species whose presence in various environments is ubiquitous and Koike et al. (2002a,b; 2006) noted the similarity

between the Red Rectangle ERE and thermoluminescence measured from gamma ray irradiated synthetic forsterite (Mg_2SiO_4). This gave an intense peak at 645–655 nm, while only very weak luminescence was observed in natural unirradiated olivine. However, other than these studies (and an apparently unpublished preprint by Koike et al. 2004 suggesting a UV excited post-thermoluminescence PL effect in irradiated forsterite, attributed by them to nano-forsterite structures), there appears to have been little experimental or theoretical work examining the possibility of silicates as ERE carriers.

Possibly related to the ERE phenomenon is the weak very broad-band structure (VBS) observed between 478 and 577 nm as a shallow depression on the interstellar extinction curve, first reported by Whiteoak (1966; see also Hayes et al. 1973; Shild 1977; van Breda & Whittet 1981; Krelowski et al. 1986). The VBS carrier has been proposed variously

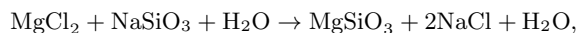
as an absorption effect (Hayes et al. 1973; Manning 1975; Huffmann 1977), extinction by a population of very small amorphous carbonaceous grains (Jenniskens 1994), or as luminescence from hydrogenated amorphous carbon (Duley & Whittet 1990).

In this paper we present PL measurements for samples of amorphous $MgSiO_3$ that have been annealed at temperatures leading up to crystallisation and show that their PL activity grows and peaks within a relatively narrow temperature range coinciding with the fragmentation of the silicate network that connects between nano-sized, but ordered domains. We suggest that silicate PL arises from non-bridging oxygen hole centres that form on the outer surfaces of the domain structures as a result of inter-domain network breakup and loss of bonded OH.

2 EXPERIMENTAL

2.1 Sample manufacture

Amorphous $MgSiO_3$ was produced by drying a sol-gel obtained by rapidly mixing 0.1 molar solutions of $MgCl_2$ and $NaSiO_3$:



the procedure for which has been described in detail elsewhere (Thompson et al. 2007, 2012). However in summary, following gelation the gels were washed and centrifuged several times in deionised water to remove the dissolved NaCl by-product. They were then dried in air at 75 °C for 24 hours. This results in large irregular glassy solids which were ground down to form a fine-grained powder. No attempt was made to control or select particle sizes, which after grinding, ranged from a few microns to several tens of microns in diameter, with a few approaching 50 to 100 μm . Separate batches of this were then annealed at discrete temperatures between 100 °C and 700 °C using a Carbolite tube furnace. The annealing time at peak temperature for each sample was $\sim 17.5 \pm 1$ hours. All characterisation measurements were subsequently performed at ambient temperature.

2.2 Data collection

2.2.1 Photoluminescence measurements

Without further preparation, approximately equal quantities of powdered sample for each of the annealing temperatures were loaded on glass microscope slides such that each sample presented a roughly circular area ~ 8 mm diameter and >0.5 mm thick. The surface was levelled off using the flat side of a stainless steel spatula. PL spectra were measured using a Horiba Jobin Yvon confocal LabRam 800 spectrometer employing 532 nm laser excitation operated at 30 mW. A 600 line spectrometer grating was used in conjunction with a 100 μm entrance slit and 300 μm confocal hole size; a 10 \times objective lens was used to both focus the incident laser spot (via imaging camera) and gather the PL radiation. In this configuration the laser spot on the sample was typically 300–400 μm in diameter, depending on the quantity of sample that lay in the focal plane. Indeed, as the overall sample surface was highly irregular due to the powder grains themselves being irregular in shape and orientation,

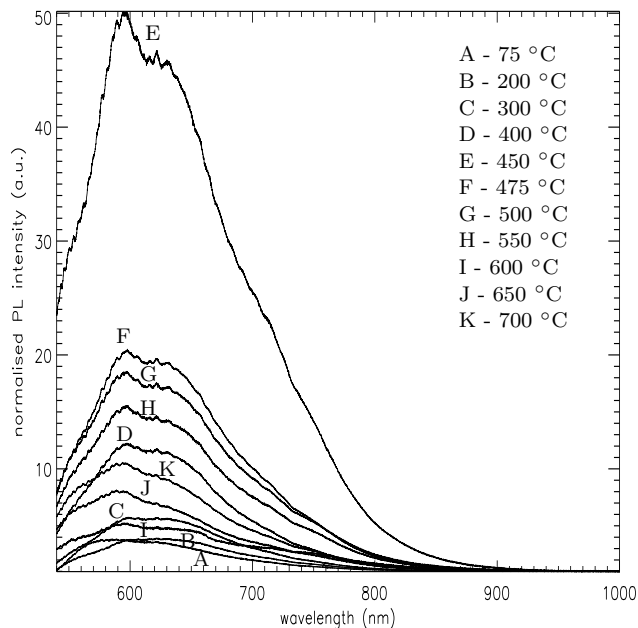


Figure 2. Normalised photoluminescence spectra for amorphous $MgSiO_3$ annealed at increasing temperatures between RT and 700 °C.

data were collected from at least ten randomly selected locations per sample and the PL spectra averaged. The spectra per location were collected in 0.051 nm steps from 534 to 1000 nm in overlapping 50 nm segments, with each segment being the average of three 3 s collections. We did not observe any systematic size dependent effects, in that spots containing numerous smaller particles tended to give similar PL profiles to those with only a few larger ones. However for any given sample, the measured intensity often showed wide variations from spot to spot, due to various physical factors, including the uneven nature of the sample surface, particle orientation, size and possible variations in the internal homogeneity of the constituent particles in respect of the PL producing species. However, all measured spectra became asymptotically flat beyond ~ 900 nm and the intensity at 1000 nm (based on an average of the 20 data points between 999 and 1000 nm) was therefore used to normalise each individual spectrum prior to averaging.

2.2.2 X-ray characterisation

Materials with structural correlations that extend only over the nanometer length-scale give only broad diffuse X-ray scattering patterns rather than sharp Bragg diffraction peaks and represent the size domain where traditional X-ray crystallographic methods become less effective. However the total scattering (TS) method, also known as the pair distribution function (PDF) method, though similar to conventional powder diffraction, provides a means of extracting structural correlations at nano-scale distances from materials that do not possess long-range periodicities (see reviews by Proffen et al. 2003, 2006; Proffen & Page 2004). Therefore, to supplement the structural analysis previously reported for these samples by Thompson et al. (2012, hereafter

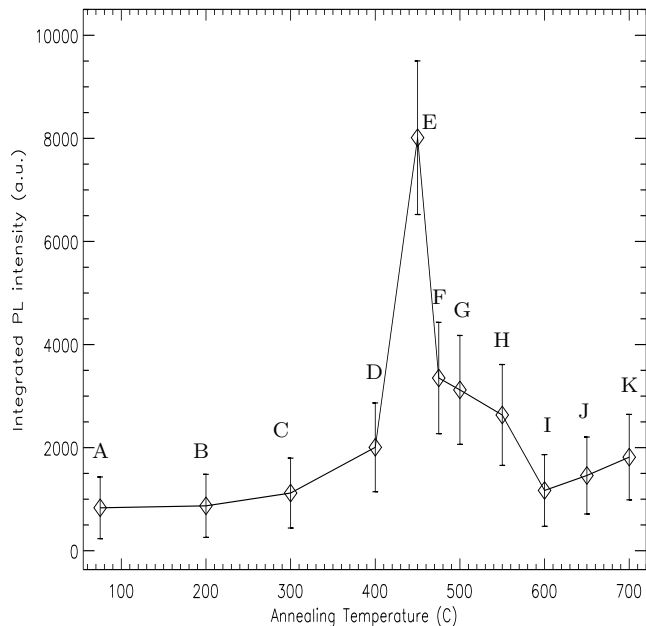


Figure 3. Integrated intensity of the PL signal for amorphous MgSiO₃ as a function of annealing temperature. Labels A to K as per fig. 1.

referred to as TPT, see summary in section 3.3), TS measurements were also made on three amorphous samples using beamline I12 at the Diamond Light Source synchrotron. These were the as-prepared sample dried at 75 °C and two that had been annealed at 300 °C and 600 °C respectively. These correspond to annealing temperatures at either side of the range where the strongest PL was observed and provide a “before and after” structural reference. Also for comparison, TS data were collected on a sample that had been extensively crystallised by annealing at 900 °C.

The main measurement criterion for TS compared to conventional powder diffraction is the need to measure to high magnitude values of the X-ray scattering vector, Q ($= 4\pi\lambda^{-1}\sin\theta$, where λ is the X-ray wavelength and θ the incident angle). This captures information relating to short-range atom–atom distances and is essential for the resolution of atomic distances by Fourier inversion (see section 3.2). The need for measuring at high Q and the weakness of the scattered signal in that region necessarily involves the use of high X-ray energies and relatively long exposure times, depending on X-ray source output characteristics. For X-rays of energy E the maximum theoretically accessible Q is $Q_{\max} = 4\pi E/hc \text{ \AA}^{-1}$. In practice however Q_{\max} is limited by the experimental geometry and detection arrangements, as is the minimum, Q_{\min} , value of Q below which data cannot be collected (e.g. limited by the backstop arrangements necessary to prevent primary beam entering the detector).

For the TS measurements samples were loaded into 2 mm Kapton capillaries and scattering data collected using 87.4 keV monochromatic X-rays produced by a 4.2 T superconducting multi-pole wiggler insertion device in the Diamond storage ring. Data collection involved 720 summed exposures per sample of 4 s each, acquired using a large pixellated 2D area detector (Thales Pixium 4343 with CsI

scintillator on amorphous Si substrate: 148 μm^2 pixel size, 2880 \times 2881 pixels; Daniels and Drakopoulos 2009). The detector was offset from the beam centre such that, at a distance of 500 mm from the sample, scattering data could be recorded out to $Q_{\max} = 30.8 \text{ \AA}^{-1}$. To provide background correction, equivalent empty capillary and air scatter measurements were also made. The scattered intensity in the form of portions of the Debye–Scherrer rings captured on the area detector for each sample was integrated to give a two dimensional data set of intensity as a function of scattering angle (converted to Q), which was then corrected for background scatter and transformed to radial distribution functions, $G(r)$ (see next section), using the PDFgetX2 software². The X-ray energy (and precise sample–detector distance) was calibrated using the measured pattern from a standard reference sample of CeO₂ of known lattice parameter.

3 RESULTS AND ANALYSIS

3.1 Photoluminescence measurements

Fig. 2 shows the averaged PL spectra for each annealing temperature. The broad PL band shows a main peak at ~ 595 nm (2.08 eV), with a weaker secondary peak at ~ 624 nm (1.98 eV). The overall strength of the band exhibits a strong variation with annealing temperatures and Fig. 3 plots the integrated PL signal for each temperature step, showing a clear peak in the PL activity around ~ 450 °C. The width of the error bars reflects the variation in measured intensity, due to both physical measurement factors (i.e. sample volume) and any intrinsic inhomogeneity in the distribution of PL centres within the silicate, as already discussed. However a clear rise in PL activity is observed above 200 °C, with a very narrow peak between 400 and 475 °C. Above this the PL activity decreases back towards the base line level at 600 °C.

3.2 Total scattering measurements

The measured TS data are shown in Fig. 4. The as-prepared and the two samples annealed at 300 and 600 °C show TS patterns characteristic of scattering from non-crystalline structures (i.e. no sharp features), while the sample annealed at 900 °C shows well defined crystalline structure, evidenced by the appearance of sharp Bragg features.

The real-space distribution, $G(r)$, of pairs of atoms within a material is described by

$$G(r) = \frac{1}{r} \frac{\sum_n \sum_m f(0)_n f(0)_m \delta(r - r_{nm})}{\langle f(0) \rangle^2} - 4\pi\rho_0, \quad (1)$$

where ρ_0 is the average atomic number density, δ is the Dirac delta function, r_{nm} is the separation of the n 'th and m 'th atoms and the sums are over all atoms in the sample. The $f(0)$'s are the atomic form factors evaluated at zero magnitude of the X-ray scattering vector Q and, to a good approximation, are given by the number of electrons, Z , on the atom. The angle brackets in the denominator indicate the average value. Thus, for a known atomic structure, $G(r)$

² <http://www.totalscattering.lanl.gov>

could be directly calculated and would consist of a series of delta functions, each at some distance r corresponding to the separation distance between two atoms. The total pair distribution function (PDF) is built up by summing over all atom-pairs in the solid.

However, $G(r)$ can be accessed experimentally through the measured TS pattern via Fourier transform,

$$G(r) = \frac{2}{\pi} \int_{Q_{\min}}^{Q_{\max}} Q[S(Q) - 1] \sin(Qr) dQ. \quad (2)$$

The Q_{\min} and Q_{\max} are defined by the experimental arrangement as described in section 2.2.2; and as wide a range in Q as possible is required, particularly in respect of Q_{\max} , in order to provide adequate real-space resolution and to decrease termination ripples in $G(r)$ at short distances, caused by the finite Q range.

In Eq. (2), $S(Q)$ is the normalized powder diffraction pattern from the sample:

$$S(Q) = \frac{I^{coh}(Q) - \sum c_i |f_i(Q)|^2}{|\sum c_i f_i(Q)|^2} + 1. \quad (3)$$

$I^{coh}(Q)$ is the coherent scattering intensity, which is the measured powder pattern once it has been corrected for experimental effects (background scattering, detector dead-time and efficiency), sample dependent effects (Compton and multiple scattering) and normalized for incident flux. The sums are over all the atomic species, i , present in the material with concentration c_i . Via this equation, $S(Q)$ and therefore $G(r)$ can be obtained from a suitably conditioned powder diffraction measurement. The definition of $S(Q)$ given above has the square of the atomic form factor in its denominator. This becomes small for X-rays at high Q and by dividing the measured intensity by this value there is a relative enhancement in the high Q scattering, which contains the valuable short-range information ignored in conventional powder diffraction analyses.

In Fig. 5, the $G(r)$ radial pair distribution functions obtained by Fourier inversion are shown for the four samples. Each peak in $G(r)$ corresponds to a discrete atom pair distance and for the sample crystallised at 900 °C atom to atom correlations clearly extend beyond the 50 Å shown in the plot. The three amorphous samples however show heavily damped $G(r)$ signals. The distance at which the oscillations in $G(r)$ diminish to zero represents the size of the coherent scattering domain (CSD) and is a measure of the distance over which the constituent atoms exhibit structural correlation. Both the as-manufactured and the 300 °C samples show a CSD size of ~30 Å, while in the 600 °C sample the CSD has reduced to ~15 Å, showing that there has been a reduction in the silicate's longer-range structural ordering as a direct result of annealing, that is, the silicate has become more amorphous.

There are two competing structural models for amorphous silicates: (i) the Zachariasen-Warren model (Zachariasen 1932, Warren 1933, 1934, Warren et al. 1936) in which Si-O tetrahedra are linked together in a statistically disordered way to form a continuous random network with no long-range periodicity; and (ii) the microcrystal model proposed by Lebiediev (1921), Randall et al. (1930a,b) and Valenkov & Porai-Koshitz (1936). Here a continuous statistically random network provides links between the surfaces

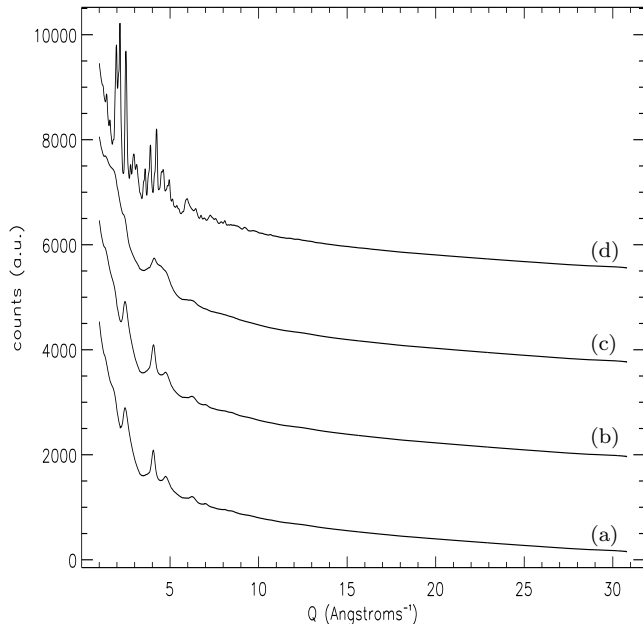


Figure 4. Measured X-ray total scattering diffraction patterns for amorphous $MgSiO_3$. (a) as manufactured (i.e. dried at 75 °C); (b) annealed at 300 °C; (c) 600 °C and (d) 900 °C.

of ultrafine microcrystalline regions (~15-20 Å) to form a domain structured material (Verweij & Konijnendijk 1976). In Fig. 5, for distances less than ~10 Å, the $G(r)$ for all three samples shows very close similarities in the silicate structure in terms of the number, shape and positions of the component peaks, showing the amorphous silicate is described well by a nano-scale domain structured model.

3.3 Summary of results from previous analyses

The evolution of short- and medium-range structure leading up to crystallisation in these samples was investigated previously by TPT using FTIR spectroscopy at 10 μm , Raman spectroscopy and X-ray scattering at low Q . The Raman and X-ray data revealed that as the annealing temperature increases, there is a build up of strain within the silicate network, which is released at ~450 °C, causing a relaxation of both the Si-O-Si bond angle and Si-O bond length. Decomposing the 10 μm band at each temperature step allowed these changes to be related to changes in the intertetrahedral connectivity. As implied by the stoichiometry of the $MgSiO_3$ composition, SiO_3 was found to be the initially dominant species and increased in proportion with rising annealing temperature as other tetrahedral species became incorporated into the SiO_3 chain structure. However in the region of ~450 °C the proportion of SiO_3 rapidly decreased as species with greater numbers of non-bridging oxygen (NBO) atoms form. This coincides with a relaxation of the strain due to the breakup, or fragmentation, of the larger chain (and sheet) structures built from interconnected tetrahedra.

The X-ray analysis performed by TPT focussed on the scattering characteristics at low Q (i.e. low scattering angle), however in Fig. 6 the conventional powder diffraction

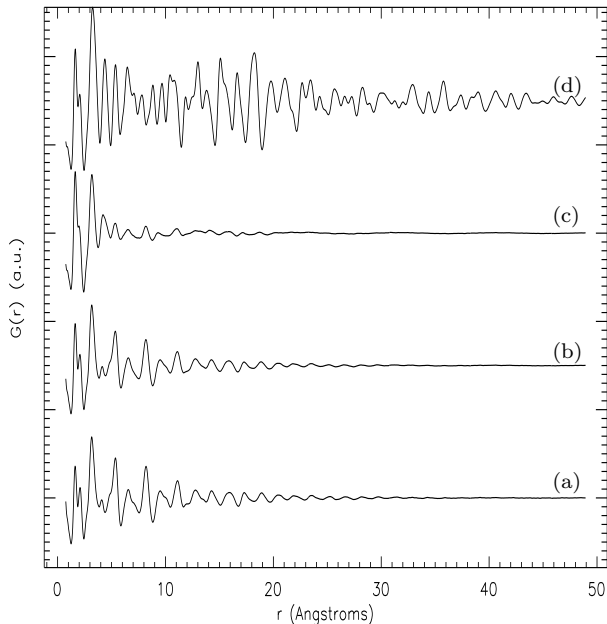


Figure 5. Radial distribution functions, $G(r)$, obtained from total scattering measurements for annealed amorphous MgSiO_3 . Labels as per Fig. 4.

data collected by TPT is plotted for a wider angular range (equivalent to 0.2 to 5 \AA^{-1} in Q), showing qualitatively the evolution of the amorphous phase and formation of crystalline structure at $\sim 650 \text{ }^\circ\text{C}$ (pattern J in the figure). These data were recorded on the I11 beamline (Thompson et al. 2009) at the Diamond Light Source using flat-plate reflection geometry and low background, high resolution Si analyser crystals. The scattering features clearly visible in the 5° to 30° 2θ range appear in the 2 to 7 \AA^{-1} range in the TS patterns of Fig. 4, albeit with lower resolution due to differences in detection arrangements. Comparing Fig. 6 with Fig. 3 shows the peak in PL activity is clearly associated with the amorphous phase. The conclusion from the TS data that the $600 \text{ }^\circ\text{C}$ sample has become less ordered is also evident in the conventional powder pattern I, which despite the presence of a few exceedingly weak trace-level Bragg features which are below the detection level of the TS area detector, shows a loss of strength for the two prominent amorphous features at 14° and 23° 2θ .

4 DISCUSSION

The annealing temperature at which PL activity becomes strongest closely coincides with the temperature at which specific modifications in the form of structural fragmentation and changing of the non-bridging oxygen distribution were previously observed to occur; and suggests a relationship between structure and PL. Below we discuss four possible mechanisms for the observed PL: formation of Si nanoparticles, impurity doping, network deformation and non-bridging oxygen hole centres, concluding that non-bridging oxygen hole centres are the likely source of the PL.

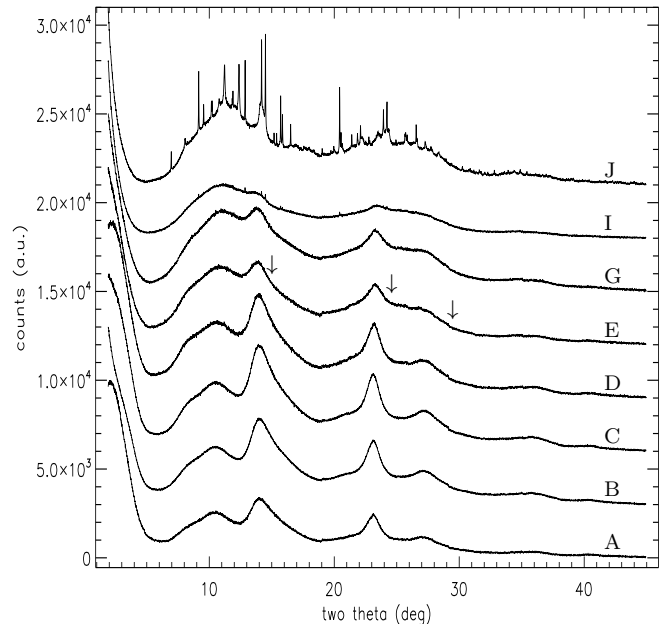


Figure 6. Conventional X-ray powder diffraction patterns for the MgSiO_3 samples measured using 15 keV X-rays at selected annealing steps. Plots are offset in y-axis for clarity, labels as per Fig. 2. The arrows shown for pattern E indicate the position of where the three strongest diffraction lines of pure-phase silicon should occur if nanocrystalline silicon is present in the sample (see section 4.1)

4.1 Embedded Si nanoparticles

Si nanoparticles (SNPs) (Witt et al. 1998; Ledoux et al. 1998, 2000, 2001, 2002) with 1.5 - 5.0 nm diameters are widely considered to be a strong contender for the ERE carrier (Witt & Vihj 2004). PL in SNPs is believed to arise from a combination of quantum confinement in nanocrystals and the passivation of dangling surface bonds by H, O, N, C, or Fe atoms to inhibit non-radiative electron-hole recombination (Kovalev et al. 1999), though the details are still debated (e.g. Hannah et al. 2012). Laboratory studies involving O and H passivation show SNPs with H-passivation and diameters of $< 2.5 \text{ nm}$ produce luminescence at blue and near-UV wavelengths, while O-passivation produces only red luminescence (Wolkin et al. 1999; Zhou et al. 2003). Because neither blue PL nor the Si-H absorption feature at $4.6 \text{ } \mu\text{m}$ are observed under interstellar conditions, O-passivation is considered more probable (Witt et al. 1998).

Once produced in a circumstellar outflow O-passivated SNPs (O-SNPs) could persist, even in the ISM with abundant H atoms, since the Si-O bond is energetically two to three times stronger than the Si-H bond. However, such particles would also contribute to the $10 \text{ } \mu\text{m}$ silicate band via Si-O vibrations and stochastically heated O-SNPs should also produce a $20 \text{ } \mu\text{m}$ emission band in excess of observationally established limits, while requiring an unrealistically high proportion of the Si abundance to be in the form of SNPs (Li & Draine 2002). In addition, experiments indicate SNPs could lose their PL capability in environments where cosmic ion bombardment is significant (Baratta et al. 2004).

These problems may be overcome if O-SNPs are either attached to, or embedded within, larger grains (Li & Draine 2002; Witt & Vijn 2004). Experiments involving embedded SNPs produced by ion implantation into solids show SNP luminescence can be preserved (e.g. Iwayama et al. 2002), but may be red-shifted (relative to PL from “free-standing” SNPs) by compressive strain imparted by the embedding matrix (Kúsová et al. 2012). X-ray absorption near edge structure (XANES) spectroscopy at the Si K-edge show the average environment surrounding the Si atoms in these silicates prior to annealing (i.e. weak PL activity) is dominated by medium-range tetrahedral Si-O symmetry (Thompson 2008) rather than cubic Si-Si environments. Fig. 7 compares the first 8 Å of the $G(r)$ obtained for the sample annealed at 600 °C (i.e. weak post-annealing PL) with theoretical $G(r)$'s calculated using the DISCUS diffuse scattering simulation software (Neder & Proffen 2008) for 2 nm spheres of crystalline silicon (Fd3m structure and 5.4307 Å lattice parameter) and crystalline enstatite (Pbca structure, lattice parameters 18.216, 8.813, 5.179 Å). Although the experimentally derived $G(r)$ contains less fine structure, reflecting its more disordered nature (crystallographic Debye-Waller temperature factors were used in the simulations), the general peak positions are quite well accounted for by the silicate structure. Peaks at 2.35 and 3.83 Å corresponding to the first and second Si-Si distances are clearly absent from the experimental $G(r)$ (and are similarly absent in the other experimentally derived $G(r)$'s).

However, there are reports in the literature regarding SNP PL in crystalline and amorphous SiO_2 induced by Si implantation (e.g. Linnros et al. 1999), so we might consider the possibility that thermally induced network fragmentation might produce SNPs, that are naturally O-passivated, via the formation and linking together of structural units with one or more dangling Si bond, somewhat akin to the Si/ SiO_2 core mantle nano grains that Li and Drain (2002) suggested could exist as ERE carriers, either as >50 Å clusters or as attachments to larger grains. The weak PL activity above ~ 600 °C however would presumably require their “reabsorption” back in to the silicate structure at higher annealing temperatures, which is plausible as the Si-Si bond dissociation energy is approximately half that of the Si-O bond. Indicated in Fig. 6 are the locations where the first three strongest peaks of crystalline cubic Si (shown by arrows at 15.1° , 24.5° and 29.4° 2θ) should appear in the conventional powder diffraction pattern for the sample annealed at 450 °C. For 2 nm Si particles the expected diffraction peak width will be at least 2° in 2θ , calculated via the well known Scherrer equation $B(2\theta) = 0.94\lambda/D \cos(\theta)$, which relates crystallite size D to the width B of a reflection of scattering angle θ . For much larger particles, any such peaks should become correspondingly narrower, however 2 nm represents a significant proportion of the CSD derived from the TS measurements and the formation of SNPs in any significant number should have an observable effect on the morphology of the conventional powder pattern. No such features are apparent in Fig. 6, suggesting SNPs do not, or cannot, form by the thermal annealing of amorphous silicate.

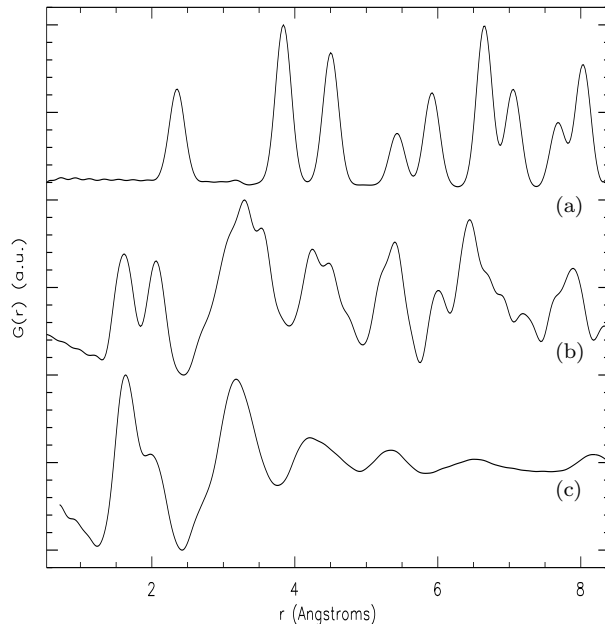


Figure 7. Calculated radial distribution functions, $G(r)$, out to 8 Å for (a) bare 2 nm diameter Si particles and (b) 2 nm silicate particles with enstatite structure compared with (c) measured $G(r)$ for the amorphous silicate annealed at 600 °C.

4.2 Impurity doping

Due to its potential technological importance (e.g. lasers Petričević et al. 1988), PL in doped crystalline forsterite (Mg_2SiO_4) and enstatite ($MgSiO_3$) have received much interest. Of relevance to the present discussion are Mn impurities since these produce luminescence lines at 630 and 670 nm in forsterite and enstatite respectively (references in MacRae & Wilson 2008) and submicron Mn-rich forsterite and enstatite crystals have been found in chondritic, porous IDPs, the matrices of chondrite meteorites (Klöck et al. 1989; Vollmer et al. 2009) and in olivine in comet 81P/Wild 2 nucleus samples (Zolensky et al. 2006), though olivine with low Fe and elevated Mn is thought to have formed from condensation in the protosolar nebula (Klöck et al. 1989). The use of high purity reagent grade starting materials ($MgCl_2 >99\%$ Fisher Scientific and $NaSiO_3$ Fluorochem) in the sol-gel procedure, although used as supplied, should rule out impurities as the source of PL. Unless annealing provides specific, but thermally temporary, structural sites for PL to be produced by impurities, any such species would be present in all samples over the temperatures studied, as should their PL. Furthermore, X-ray fluorescence spectra (Horiba XGT-7000 X-ray Fluorescence Microscope) collected from different regions of a portion of the as-prepared sample showed no lines in the region of 6 keV characteristic of Mn K_α fluorescence. The observation by Koike et al. (2002a,b 2006) that luminescence can be induced in forsterite that has been structurally disrupted by gamma rays likely points to an intrinsic structure related mechanism.

4.3 Network deformation

Shinno et al. (2000) observed luminescence in crystalline forsterite subjected to shock pressures in the range of 10 to 82 GPa. Correlating shifts in the Mg-O translational and Si-O rotational Raman bands at 308 and 328 cm^{-1} with the growth of luminescence intensity as a function of pressure, they attributed the luminescent mechanism to lattice deformation, which allows transitions to occur between deformed electron levels and vibrational sublevels in the $[\text{SiO}_4]^{4-}$ molecular orbital (Shinno et al. 1999). In TPT shifts to higher frequency in the position of the 670 cm^{-1} Raman band, attributable to a narrowing of the Si-O-Si intertetrahedral bond angle, ϕ_{T-T} , and a stretching of the Si-O bond length, $r_{\text{Si-O}}$ (also deduced by TPT from X-ray scattering), indicate that the silicate structure becomes increasingly strained with annealing temperature. Fig. 8 reproduces the TPT Raman data. Clearly visible is a general trend towards higher frequency, but with anomalously large shifts in the region of 450 °C. The sudden decrease in frequency between 475 and 500 °C represents the release of built up strain by structural re-ordering and changes in the relative abundances of SiO_2 , Si_2O_5 , SiO_3 , Si_2O_7 and SiO_4 species within the silicate (see TPT for detailed discussion). The peak in PL activity also coincides with the peak in strain at ~ 450 °C, suggesting a possible link. However, the luminescence observed by Shinno et al. peaked at ~ 400 nm, with a long tail decay showing little activity by 600 nm and was the result of high pressure deformation, which seems unlikely to be replicated by the relatively low temperatures used here. Furthermore forsterite, although known to be the first crystalline phase to form in amorphous MgSiO_3 (Rietmeijer et al. 1986; Thompson & Tang 2001; Roskosz et al. 2009), contains isolated SiO_4 tetrahedra while the 670 cm^{-1} Raman band relates to changes in the intertetrahedral bond angle ϕ_{T-T} and therefore strain within linked tetrahedral structures. However, the close occurrence of the two peaks in PL activity and strain in the region of 450 °C means that we cannot necessarily rule out a deformation-based contribution to the PL (see section 4.5).

4.4 Non-bridging oxygen hole centres (NBO-HC)

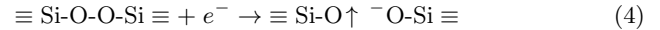
Due to its industrial and commercial importance, most studies of luminescence defect centres in undoped silicate focus on SiO_2 , where four intrinsic types have been identified: (i) the E' centre due to either a paramagnetic positively charged oxygen vacancy $\equiv\text{Si}\cdot\text{Si}\equiv$ (where $\equiv\text{Si}$ represents the bonding to three other oxygen atoms in the Si-O tetrahedron), or to a neutral dangling silicon bond $\equiv\text{Si}\cdot$; (ii) a dangling oxygen bond $\equiv\text{Si}\cdot\text{O}\cdot$ which is the NBO-HC; (iii) a peroxy radical (POR) $\equiv\text{Si}\cdot\text{O}\cdot\text{O}$ and (iv) oxygen deficiency centre (ODC) due either to a neutral oxygen vacancy $\equiv\text{Si}\cdot\text{Si}\equiv$ or twofold-coordinated silicon atom $\equiv\text{Si}\cdot\text{O}\cdot\text{Si}\cdot\text{O}\cdot\text{Si}\equiv$. Of these only the POR and NBO-HC defects produce PL in the region of 2 eV (Skuja 1998).

POR defects can be formed by the combination of $\equiv\text{Si}\cdot E'$ centres with interstitial O_2 molecules (Edwards & Beall-Fowler 1982). Re-examination of the TPT Raman data collected at each annealing step shows no Raman feature in the region of 1549 cm^{-1} , that would be characteristic of inter-

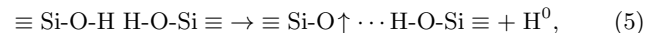
stitial O_2 (Skuja et al. 1998). The rise in PL with annealing is therefore unlikely to be due to POR defects.

Deconvolution of the mid-IR 10 μm band by TPT showed the strain release peak at ~ 450 °C to coincide with a significant change in the relative proportions of the various tetrahedral species within the silicate, while changes in the silicate's IR hydration band near 3 μm suggested this was likely driven or facilitated by dehydrogenation of the sample. Consequently, the PL may be related to the formation of defects in the silicate structure resulting from this process.

In naturally occurring terrestrial silicate minerals single, or multi-step, dehydroxylation occurs in the range 500-700 °C. However, The specific dehydroxylation temperature is determined primarily by the mineral's specific crystal structure and it's octahedral and extra-framework cation compositions, with various intermediary crystal phases forming as dehydroxylation progresses (e.g. Che et al. 2011 and references therein). Furthermore, the dehydroxylation temperature is lowered if the mineral structure becomes disordered (Tyburczy & Ahrens 1988) such that the structural changes seen here and by TPT are likely to be related to the loss of bonded OH. In amorphous SiO_2 PL bands are observed at 629 nm (1.97 eV) and 590 nm (2.1 eV) and are due, respectively, to the following reactions (Munekuni et al. 1990):



and



In reaction (4) the $\equiv\text{Si}\cdot\text{O}^-$ anion, once excited, acts as an energy donor, transferring its excess energy to the NBO-HC energy acceptor defect that has been formed together with the $\equiv\text{Si}\cdot\text{O}^-$. The NBO-HC is then pumped to the excited state, returning to the ground state by luminescence. Reaction (5) on the other hand requires the existence, or formation, of closely located $\equiv\text{Si}\cdot\text{O}\cdot\text{H}$ pairs from which a hydrogen atom is released to leave a hydrogen bonded NBO-HC. The two peaks in the PL spectrum at 595 and 624 nm (2.08 and 1.98 eV respectively) of our samples are very close to the SiO_2 NBO-HC PL peak energies and therefore suggest a similar NBO-HC origin. To support this, Fig. 9 compares PL spectra measured for samples of commercially sourced silica (amorphous SiO_2), mineral enstatite and two mineral olivines. All three exhibit clear PL features, albeit with weak activity, close to 590 and 630 nm and similar to those observed in the spectra of the annealed amorphous silicate.

Fig. 10 plots the percentage of NBO atoms in the silicate for each annealing temperature. These are derived from the relative proportions of the SiO_3 , Si_2O_7 , Si_2O_5 and SiO_4 obtained by TPT by decomposition of the 10 μm band. There is a ~ 10 % increase in the NBO content between 200 °C and 475 °C which, taken in combination with the reduction in the CSD size, implies a breaking of intertetrahedral connections. Since the core structure of the CSD remains unchanged this can be viewed either as a "surface" fragmentation of the structured domains, or as a growth and penetration of the random interdomain network into the ordered domains. We suggest therefore that during this process

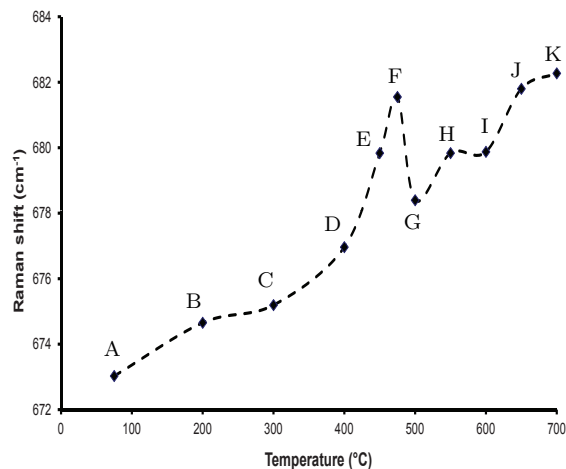


Figure 8. Shift in peak position of $MgSiO_3$ 670 cm^{-1} medium-range order Raman feature as a function of annealing temperature. Shifts towards higher frequencies are characteristic of a narrowing of the Si-O-Si bond angle and a shortening of the Si-O bond distance. The sharp decrease between 475 and 500 C is attributed to strain release. Labels as per Fig. 2.

NBO-HC defects, associated with newly formed NBO sites around the domain surface, give rise to the observed PL.

4.5 Astrophysical relevance

Due to their formation in H-rich environments, bonded hydrogen defects such as SiH and SiOH have long been believed to be present in cosmic silicates (e.g. Moore et al. 1991; Whittet et al. 1997; Timmermann & Larson 1993; Malfait et al. 1999; Thompson et al. 2003) though the close proximity of O-H features from water ice have hindered observational identifications. Hydroxylated amorphous silicates on the other hand have been identified in interplanetary dust particles (IDPs) and glasses with embedded metal and sulphides (GEMS; Thomas et al. 1993; Bradley 1994; Bradley et al. 2005) some of which may be pre-solar (Messenger et al. 2003) and originate from the ISM (Bradley et al. 1999). The presence of OH groups in these recovered amorphous silicates is thought to result from hydrogen implantation by irradiation processes (Bradley 1994); while laboratory work by Djouadi et al. (2011) shows stable OH defects in ISM silicates should result from low energy proton irradiation in shock waves.

In a crystalline silicate the total number of hydroxylated sites is small due to the limited surface area of the crystal edge regions where OH can form, thus limiting the number of potential NBO-HC sites and hence yield only the low levels of PL activity observed in mineral species. In amorphous silicates however the inherent disorder, possibly further supplemented by the disruptive effects of ion implantation (Demnyk et al. 2001, 2004; Brucato et al. 2003; Jäger et al. 2003;

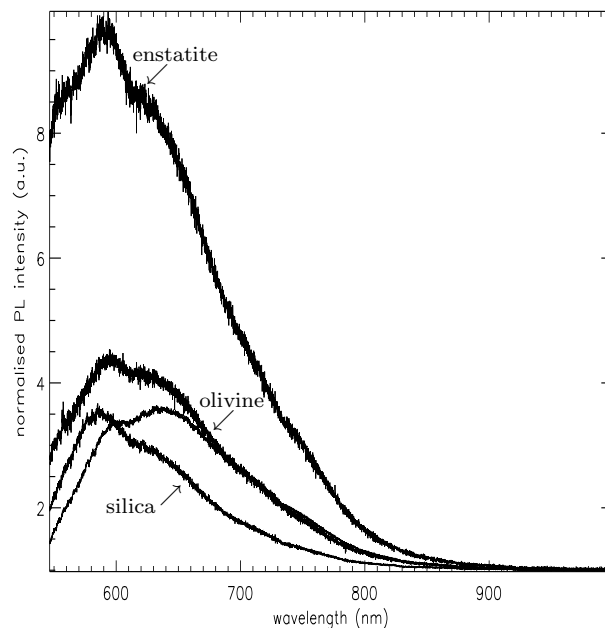


Figure 9. PL measured for Silica, mineral enstatite and two olivine mineral samples.

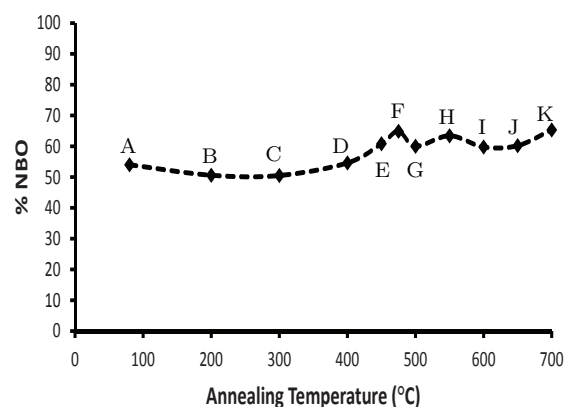


Figure 10. Percentage of non-bridging oxygen atoms in the $MgSiO_3$ silicate at each annealing temperature. Labels as per Fig. 2.

Bringa et al. 2007; Davoine et al. 2008) should provide for greater numbers of OH edge defects capable of producing NBO-HC's when annealed and, hence, an increase in PL activity. The level of PL produced by silicate grains in a potential ERE environment will thus depend on whether the grains have experienced (a) sufficient hydrogenation to produce bonded OH and (b) sufficient thermal processing at

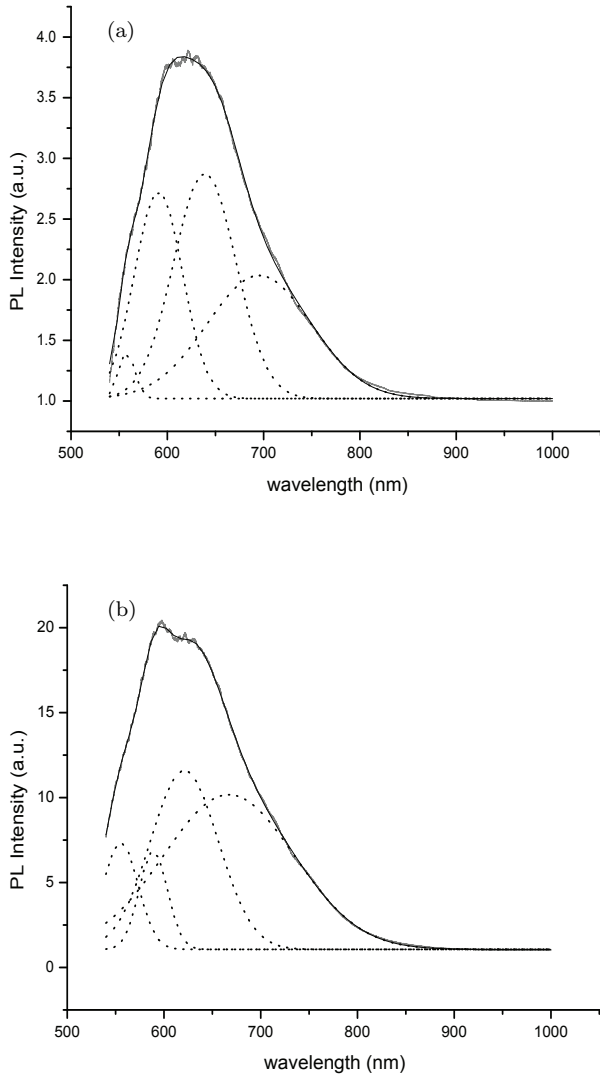


Figure 11. Gaussian decomposition for the PL spectra for amorphous MgSiO_3 (a) annealed at $200\text{ }^\circ\text{C}$ and (b) annealed at $475\text{ }^\circ\text{C}$. Component peaks for (a) are located at 557.64, 590.91, 639.00 and 695.42 nm (2.223, 2.098, 1.940 and 1.783 eV respectively) and for (b) are located at 554.07, 587.54, 621.03 and 659.99 nm (2.238, 2.110, 1.996 and 1.879 eV respectively).

some point to convert these to NBO-HC's (and would not necessarily have to have occurred in situ within the ERE emitting environment). Observationally, silicate PL should thus correlate with weakened, or absent, silicate OH features in the mid-IR.

The change in the relative distribution of tetrahedral species observed by TPT and the domain structure reported here raises the possibility that NBO-HC defects could form in different regions of the silicate structure rich in one or other of the Si-O species. Indeed the large error bars in the integrated PL intensity, particularly for the $450\text{ }^\circ\text{C}$ sample, arise from the increased variation in the measured PL signal obtained for different spots on the powder sample; and likely indicates phase inhomogeneity caused, or exacerbated, by

annealing. These slightly different structural environments could offer a means of tuning both the PL band width and its peak wavelength in different environments. In Fig. 11 we show the results of a Gaussian decomposition of the PL bands measured for the samples annealed at $200\text{ }^\circ\text{C}$ and $475\text{ }^\circ\text{C}$ (label F in Figs. 2 and 3). Four components were necessary to reproduce the measured signal and were located at 554.07, 587.54, 621.03 and 659.99 nm (2.24, 2.11, 1.99 and 1.88 eV respectively). A similar fit to the $200\text{ }^\circ\text{C}$ band gave component positions of 559.52, 593.27, 632.70 and 641.87 nm (2.22, 2.09, 1.96 and 1.93 eV respectively) which, with reference to Fig. 8 represent points of high and low strain. In both cases the energies are sufficiently close to the energies of reactions 4 and 5 to suggest that four distinct NBO-HC environments may be contributing to the PL. That the relative numbers of these can vary is also apparent in Fig. 9, where the weak shoulder at $\sim 554\text{ nm}$ visible in the annealed samples in Fig. 1 is more pronounced in the mineral enstatite spectrum compared to either the olivine or silica spectra. On the other hand, the weaker $\sim 659\text{ nm}$ feature in both the annealed samples and the enstatite and silica spectra is more prominent in one of the olivine spectra. As is the case with embedded SNPs these small variations in energy may be related to strain in the surrounding silicate network in which the two generic NBO-HCs are embedded, which could affect the local symmetry to possibly produce four distinct sites, or contribute directly to their formation (Hibino & Hanafusa 1988).

From the foregoing, the narrow temperature range over which the PL activity peaks appears to be clearly related to the thermally driven evolution of an initially hydrated amorphous structure, with initial changes in the number of NBOs allowing PL active NBO-HCs to form. As these structural changes continue towards crystallisation, the PL activity decreases as the NBO-HC defects become “reabsorbed” back into the silicate structure. Therefore, increased PL activity is a characteristic of amorphous grain processing prior to crystallisation. As such, ERE due to silicate PL should be anti-correlated with IR features due to crystalline grains. The range in temperature reported here over which PL is observed however could be widened if the PL-reducing effects of thermal annealing are offset by structural disruption and rehydrogenation due to ongoing ion implantation.

Comparing Figs. 1 and 2 suggests that the silicate PL, peaking at $\sim 650\text{ nm}$, better matches the ERE from the Red Rectangle protoplanetary nebula (Fig. 1a) rather than the ERE from the two reflection nebulae (Fig. 1c and 1d), where the peak wavelength is shifted longward to $\sim 700\text{ nm}$, though the low resolution spectrum for the NGC7027 planetary nebula (Fig 1b) is suggestive of a component close to 650 nm . One possibility for the peak position variability observed from source to source is that ERE does not originate from a single specific carrier, but rather a set of different carriers whose specific PL producing properties (e.g. relative abundance, size distribution etc.) is determined by local conditions (A. N. Witt, personal communication). In this respect, silicate PL at $\sim 650\text{ nm}$ may represent one component of a wider ERE producing grain population and may contribute to a lesser or greater extent in different sources.

Finally, silicate PL via NBO-HC's should not produce excess contributions to the mid-IR 10 and $20\text{ }\mu\text{m}$ bands as, unlike O-SNPs, an additional vibrating Si-O species is not

invoked. It may be possible however that luminescence from silicates could be observable at other wavelengths. Koike et al. (2006) observed blue-shifted thermoluminescence in samples of forsterite and fused quartz that had been neutron irradiated. Although the luminescence mechanism was not identified, peak emission occurred between 340 – 500 nm and 420 – 520 nm, respectively, both of which are close, for example, to the interstellar VBS observed between 478 and 577 nm. We may therefore speculate that the formation of stable defects in silicate grains, akin to those outlined in section 4.4, might also give rise to other observable emissions outside of the ERE region.

5 CONCLUSIONS

We have observed the rise and decline of PL activity in thermally processed amorphous $MgSiO_3$ and identify this with the formation and reabsorption of non-bridging oxygen hole centres which form when intertetrahedral connections are broken and reformed as a result of structural rearrangement and dehydroxylation. Decomposition of the PL band suggest ~ 4 distinct defects are contributing to the observed PL signal, which we interpret as being due to hole centres associated with regions of differing tetrahedral connectivity, while differences in their PL energies may be related to distortions of the hole centre environment by strain within the silicate network. X-ray scattering shows ordered nanocrystalline domains to be present within the silicate, whose size is reduced with annealing, suggesting that the non-bridging oxygen hole centres most likely form around the shrinking surface of the nanocrystal domains as it becomes incorporated into the random network structure that links between the domains. As crystallisation proceeds, the hole centres become reabsorbed into the structure and PL activity decreases. The formation of non-bridging oxygen hole centres requires the presence of hydrogen atoms in the form of bonded OH molecules and can be achieved either by formation in H-rich environments and/or by implantation. If astronomical red PL, i.e. ERE, originates (or at least in part) from silicates, then its presence will be indicative of hydrated grains having, at some point in their history, undergone low-level thermal processing; while its absence may indicate anhydrous grains and/or grains that have undergone extensively thermal processing. Differences in the PL emission characteristics may derive naturally from differences in structural state, compositional variation or differing H implantation conditions.

ACKNOWLEDGMENTS

This work was supported by Diamond Light Source through beamtime award 7124. SJD acknowledges financial support from Diamond Light Source and Keele University. The authors would also like to extend their thanks to Professor A.N. Witt for providing the ERE data for NGC7023 and additional discussions regarding ERE; and to Professor L. d’Hendecourt for his helpful comments and suggestions during review.

APPENDIX

Quantities and definitions

CSD	coherent size domain
ERE	extended red emission
E'	colour centre due to missing oxygen atom
GEMS	glasses with embedded metal and sulphides
$G(r)$	atomic pair distribution function (PDF)
NBO	non-bridging oxygen (atom)
NBO-HC	non-bridging oxygen hole centre
ODC	oxygen deficiency centre
O-SNP	oxygen passivated silicon nano particle
PDF	(atomic) pair distribution function ($G(r)$)
ϕ_{T-T}	inter-tetrahedral bond angle
PL	photoluminescence
POR	peroxy radical
Q	X-ray scattering vector
r_{Si-O}	silicon to oxygen bond length
$S(Q)$	normalised scattered intensity
SNP	silicon nano particle
TPT	Thompson, Parker & Tang (2012)
TS	total (X-ray) scattering
VBS	very broad-band structure
XANES	X-ray absorption near edge structure

REFERENCES

- Berné O., Joblin C., Rapacioli M., et al., 2008, *A&A*, 479, L41
 Baratta G. A., Strazzulla G., Compagnini G. and Longo P., 2004, *Appl. Surface Sci.*, 226, 57
 Bradley J. P., 1994, *Science*, 265, 925
 Bradley J. P., Keller L. P., Snow T. P., et al., 1999, *Science*, 285, 171
 Bradley J. P., Dai Z. R., Erni R., et al., 2005, *Science*, 307, 244
 van Breda I. G. and Whittet D. C. B., 1981, *MNRAS*, 195, 79
 Bringa E. M., Kucheyev S. O. and Loeffler M. J., 2007, *ApJ*, 662, 372
 Brucato J. R., Strazzulla G., Baratta G. and Colangeli L., 2003, *A&A* 413, 395
 Chang H.-C., Chen K. and Kwok S., 2006, *ApJ*, 639, L63
 Che C., Glotch T. D., Bish D. L., et al., 2011, *JGR* 116, E05007
 Daniels J. E. and Drakopoulos M., 2009, *J. Synchrotron Rad.*, 16, 463.
 Darbon S., Perrin J. -M. and Sivan J. -P. 1999, *A&A*, 348, 990
 Davoisine C., Leroux H. and Frère M., 2008, *A&A*, 482, 541
 Demyk K., Carrez Ph., Leroux H., et al., 2001, *A&A*, 368, L38
 Demyk K., d’Hendecourt L., Leroux H., et al., 2004, *A&A*, 420, 233
 Djouadi Z., Robert F., Le Sergeant d’Hendecourt L, et al., 2011, *A&A* 531, A96
 Draine B. T., 2003, *ARAA*, 41, 241
 Duley W. W., 1985, *MNRAS*, 215, 259
 Duley W. W., 1988, *Ap&SS*, 150, 387
 Duley W. W., 2001, *ApJ*, 553, 575
 Duley W. W. and Whittet D. C. B., 1990, *MNRAS*, 242, 40P
 Duley W. W. and Williams D. A., 1988, *MNRAS*, 230, 1P
 Duley W. W., Sehra S. and Williams D. A., 1997, *ApJ*, 482, 866
 Edwards A. H. and Beall-Fowler W., 1982, *Phys. Rev. B*, 26, 6649
 Furton D. G. and Witt A. N., 1990, *ApJ*, 364, L45
 Furton D. G. and Witt A. N. 1992, *ApJ*, 386, 587
 Godard M. and Dartois E. 2010, *A&A*, 519, A39
 Gordon K. D., Witt A. N. and Friedmann B. C. 1998, *ApJ*, 498, 522

- Hannah D. C., Yang J., Podsiadlo P. et al., 2012, *Nano Lett.*, 12, 4200
- Hayes D. S., Mavko G. E., Radick, R. R., et al., 1973. In *Interstellar Dust and Related Topics*, J. M. Greenberg and H. V. Van de Hulst (eds.) 83
- Hibino Y. and Hanafusa H., 1988, *J Non-Cryst. Solids*, 107, 23
- Iwayama T. S., Hama T., Hole D. E. and Boyd, I. W., 2002, *Surf. & Coatings Technology*, 158-159, 712
- Jäger C., Fabian D., Schrepel F., et al., 2003, *A&A*, 401, 57
- Jenniskens P., 1994, *A&A*, 284, 227
- Kerr T. H., Hurst M. E., Miles J. R., Sarre P J., 1999, *MNRAS*, 303, 446
- Löck W., Thomas K. L., McKay D. S. and Palme H., 1989, *Nature*, 339, 126
- Koike K., Nakagawa M., Koike C., et al., 2002a, *A&A*, 290, 1133
- Koike C., Chihara H., Koike K., et al., 2002b, *Meteor. Planet. Sci.*, 37, 1591
- Koike K., Chihara H., Koike C. et al., 2004, arXiv:astro-ph/0403540v1
- Koike K., Nakagawa M., Koike C., et al., 2006, *Planet. Space Sci.*, 54, 325
- Kovalev D., Heckler H., Polisski G. and Koch F., 1999, *Phys. Status Solidi B*, 215, 871
- Krelowski J., Maszkowski R., Strobel A., 1986, *A&A*, 166, 271
- Kurth M, Witt A. N., Vijh U, P. and Barns F. S., 2013, *BAAS*, 22144006
- Kůsová K., Ondič L., Klimešová E. et al., 2012, *Appl. Phys. Lett.*, 101, 143101
- Lebiediev A. A. 1921, *Trans. Opt. Inst. Petr.*, 2, 10
- Ledoux G., et al. 1998, *A&A*, 333, L39
- Ledoux G., Guillois O., Porterat D., et al., 2000, *Phys. Rev. B.*, 62 (23), 15942
- Ledoux G., Gong J., Huisken F., et al., 2002, *Appl. Phys. Lett.*, 80 (25), 4834
- Ledoux G., Guillois O., Huisken F., et al., 2001, *A&A*, 377, 707
- Linnros J., Lalic N., Galeckas A. and Grivickas V., 1999, *J. Appl. Phys.*, 86, 6128
- Li A. and Draine, B. T. 2002, *ApJ*, 564, 803
- MacRae C. M. and Wilson N. C., 2008, *Microscopy & Microanalysis*, 14, 184
- Malfait K., Waelkens C., Bouwman J., et al., 1999, *A&A*, 345, 181
- Manning P. G., 1975, *Nature*, 255, 40
- Messenger S., Keller L. P., Stadermann F. J., et al., 2003, *Science*, 300, 105
- Moore M. H., Tanabe T. and Nuth J. A., 1991, *ApJ*, 373, L31
- Munekuni S., Ymanaka T., Shimogaichi Y., et al., 1990, *J. Appl. Phys.*, 68, 1212
- Neder R. B. and Proffen Th., 2008. *Diffuse scattering and defect structure simulations*. IUCr Texts on Crystallography 11, Oxford University Press, Oxford.
- Petričević V., Gayen S. K., Alfano R. R. et al., 1988, *Appl. Phys. Lett.*, 52, 1040
- Proffen Th. and Page K. L., 2004, *Z. Kristallogr.*, 219, 130
- Proffen Th., Billinge S. J. L., Egami T. and Louca D., 2003, *Z. Kristallogr.*, 218, 132
- Proffen Th., Page K. L., McLain S. E., et al., 2006, *Z. Kristallogr.*, 220, 1002
- Randall J. T., Rooksby H. P. and Cooper B. S., 1930a, *J. Soc. Glass Technol.*, 14, 219
- Randall J. T., Rooksby H. P. and Cooper B. S., 1930b, *Z. Krist.*, 75, 196
- Rhee Y., Lee T., Gudipati M., et al., 2007, *PNAS*, 104, 5274
- Rietmeijer F. J. M., Nuth J. A. and MacKinnon I. D. R., 1986, *Icarus*, 66, 211
- Roskosz M., Gillot J., Capet F., et al., 2009, *Ap J*, 707, L174
- Sakata A., Wada S., Narisawa T., et al., 1992, *ApJ*, 393, L83
- Scott A. D., Evans A. and Rawlings J. M. C., 1994, *MNRAS*, 269, L21
- Seahra S. S. and Duley W. W., 1999, *ApJ*, 520, 719
- Schmidt G. D., Cohen M. and Margon B., 1980, *ApJ*, 239, L133
- Schild R. E., 1977, *AJ*, 82, 337
- Shinno I., Nakamura T. and Sekine, T., 1999, *Mineral. J.*, 21, 119
- Shinno I., Nakamura T. and Sekine, T., 2000, *J. Luminescence*, 87-89, 1292
- Skuja L., 1998, *J Non-Cryst. Solids*, 239, 16
- Skuj, L., Güttler B., Schiel D. and Silin A., 1998, *J. Appl. Phys.*, 83, 6106
- Smith T. L. and Witt A. N., 2002, *ApJ*, 565, 304
- Szomoru A. and Guhathakurta P., 1998, *Apj*, 494, L93
- Thomas K. L., Blanford G. E., Keller L. P., et al., 1993, *Geochim. Cosmochim. Acta*, 57, 1551
- Thompson S. P., 2008, *A&A*, 484, 251
- Thompson S. P. and Tang, C. C., 2001, *A&A*, 368, 721
- Thompson S. P., Fonti, S., Verrienti, C., et al., 2003, *Meteor. Planet. Sci.*, 38, 457
- Thompson S. P., Verrienti, C., Fonti, S., et al., 2007, *Adv. Space Res.*, 39, 375
- Thompson S. P., Parker J. E., Potter J., et al., 2009, *Rev. Sci. Instr.*, 80, 075107
- Thompson S. P., Parker J.E. and Tang C. C., 2012, *A&A*, 545, A60 (TPT)
- Timmermann R. and Larson H. P., 1993, *ApJ*, 415, 820
- Tyburczy J. A. and Ahrens T. J., 1988, *Proc. Lunar Planet. Sci. Conf.*, 18th, 435
- Valenkov N. and Porai-Koshitz E. 1936, *Z. Krist.*, 95, 195.
- Verweij H. and Konijnendijk W. L., 1976, *J. Am. Ceramic Soc.*, 59, 517
- Vollmer C., Brenker F. E., Hoppe P. and Stroud, R. H., 2009, *ApJ*, 700, 774
- Wada S., Mizutani Y., Narisawa T. and Tokunaga A. T., 2009, *ApJ*, 690, 111
- Warren B. E., 1933, *Z. Krist.*, 86, 349
- Warren B. E., 1934, *J. Am. Ceram. Soc.*, 17, 249
- Warren B. E., Krutter H. and Morningstar O., 1936, *J. Am. Ceram. Soc.*, 19, 202
- Waters L. B. F. M., et al. 1998, *A&A*, 331, L61
- Webster A., 1993, *MNRAS*, 264, L1
- Whiteoak J. B., 1966, *ApJ*, 144, 305
- Whittet D. C. B., Boogert A. C. A., Gerakines P. A., et al. 1997, *ApJ*, 490, 729
- Witt A. N. and Boroson T. D., 1990, *ApJ*, 355, 182
- Witt A. N. and Schild R. E., 1988, *ApJ*, 325, 837
- Witt A. N., and Vijh, U. P., 2004, in *ASP Conf. Ser.*, 309, *Astrophysics of Dust*, ed. A. N. Witt, G. C. Clayton and B T. Draine (San Francisco: ASP), 115
- Witt A. N., Gordon K. D. and Furton D. G., 1998, *ApJ*, 501, L111
- Witt A. N., Gordon K. D., Vijh U. P., et al. 2006, *ApJ*, 636,303
- Witt A. N., Mandel S., Sell P. H., et al., 2008, *ApJ*, 679, 497
- Wolkin M. V., Jorne J., Fauchet, P. M., et al., 1999, *Phys. Rev. Lett.*, 82, 197
- Zachariasen W. H., 1932, *J. Am. Ceram. Soc.*, 17, 3841
- Zhou Z., Brus L. and Friesner R., 2003, *Nano Lett.*, 3, 163
- Zolensky M. E., Zega T. J., Yano H., et al., 2006, *Science*, 314, 1735

This paper has been typeset from a $\text{\TeX}/\text{\LaTeX}$ file prepared by the author.